IEEE Transactions on Power Electronics

Optimal Design of Integrated Magnetics for Differential Rectifiers and Inverters

Journal:	*IEEE Transactions on Power Electronics*
Manuscript ID	TPEL-Reg-2017-02-0313
Manuscript Type:	Regular Paper
Date Submitted by the Author:	16-Feb-2017
Complete List of Authors:	Wu, Minxin; University of Hong Kong Li, Sinan; The University of Hong Kong, Department of Electrical & Electronic Engineering Tan, Siew-Chong; University of Hong Kong, Electrical and Electronic Engineering Hui, S. Y. (Ron); The University of Hong Kong, Department of Electrical & Electronic Engineering
Keywords:	Power electronics, AC-DC power conversion

SCHOLARONE™
Manuscripts

For Review

OPTIMAL DESIGN OF INTEGRATED MAGNETICS FOR DIFFERENTIAL RECTIFIERS AND INVERTERS

Minxin Wu[1], Sinan Li[1], *Member, IEEE,* Siew Chong Tan[1], *Senior Member, IEEE,* and S. Y. R. Hui[1,2], *Fellow, IEEE*

[1] Department of Electrical & Electronic Engineering, The University of Hong Kong, Hong Kong

[2] Department of Electrical & Electronic Engineering, Imperial College London, London, UK

***Abstract*— In this paper, a type of low-frequency integrated AC inductor without inductance coupling is proposed for differential rectifiers/inverters. The objective is to increase the power density of these converters by replacing their two bulky and low-frequency AC inductors with the proposed integrated AC inductor, which is much more compact. The principles of the proposed magnetic integration approach and the optimization procedures are explained in detail. An integrated inductor with 34.9% reduction in volume as compared to its discrete-inductor counterpart is designed and tested via simulations using the software Maxwell. Three integrated inductor prototypes with a core volume reduction of up to 30.9% are constructed in the laboratory and are applied to a buck differential rectifier for experimental verification. Their performance in terms of coupling effect, thermal temperature, power efficiency and system switching frequency are examined.**

I. INTRODUCTION

A differential rectifier/inverter comprising two differentially-connected DC/DC converters with bidirectional power flow capability is a popular solution for achieving AC/DC and/or DC/AC power conversion [1]. Fig. 1 shows the general circuit configuration of a differential rectifier/inverter, in which the two bidirectional DC/DC converters are connected in series at the AC side and in parallel at the DC side. Typically, the two bidirectional DC/DC converters are identical ones and a myriad of topologies such as buck, boost, and buck-boost converters can be selected, depending on specific applications. The inherent features of such differential type of converters are (i) there bridgeless structure which indicates high power efficiency for high power applications, (ii) possibility of direct

For Peer Review

voltage step-up/down without an additional DC/DC conversion stage, (iii) feasibility of performing active ripple-power decoupling (for eliminating the conventional power-buffering dc-link electrolytic capacitor that has a short service lifetime) without adding extra components, and (iv) low leakage current between the AC and the DC side [1]–[9]. Due to these features, differential rectifiers/inverters have been extensively reported and applied in many applications, e.g., LED driving [2], uninterruptible power supplies (UPSs) [3], fuel cell and photovoltaic (PV)-based inverters [4], [5].

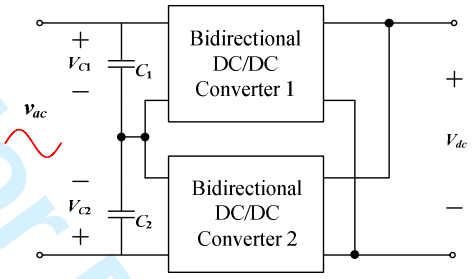
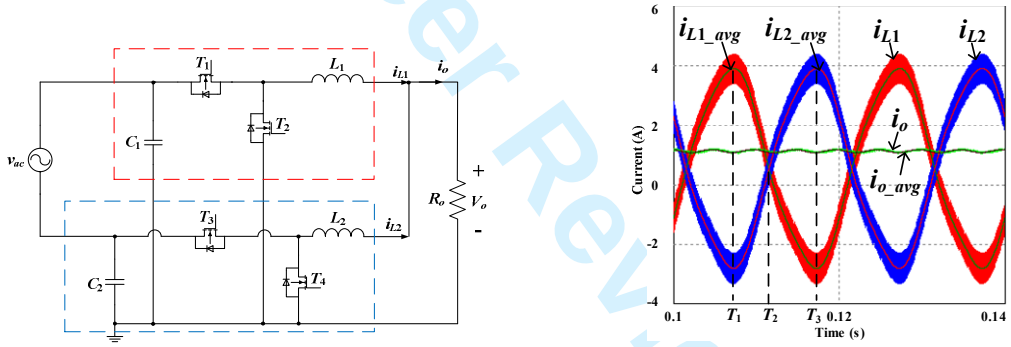


Fig. 1. General configuration of a differential rectifier/inverter.



(a) (b)

Fig. 2. (a) Buck differential rectifier and (b) the inductor currents and output current of the buck differential rectifier (v_{ac} =110 Vrms/ 50 Hz, $C_1 = C_2 = 15$ μF, $R_o = 39$ Ω, $L_1 = L_2 = 3.5$ mH, $P_o = 50$ W).

Despite the advantages, a differential rectifier/inverter typically requires the use of two bulky low-frequency inductors either at the AC side or at the DC side of the converter, which significantly reduces the power density of the system. The reason for employing two bulky inductors is explained here based on an exemplary buck-type differential rectifier as shown in Fig. 2(a) [2], where two inductors L_1 and L_2 are connected in parallel at the DC output. As illustrated in Fig. 2(b), while the

For Peer Review

output current i_o is almost DC, the currents flowing through L_1 and L_2 (i_{L1} and i_{L2}) contain strong line-frequency components. It should be noticed that the low-frequency components are inherent due to the differential structure of the converter and cannot be mitigated by employing a higher switching frequency. In particular, i_{L1} and i_{L2} can reach a peak current level several times higher than their DC components. To avoid magnetic core saturation caused by the high peak currents, the cross-sectional area and thus the overall volume of L_1 and L_2, must be sufficiently large if two discrete magnetic cores are employed to construct L_1 and L_2.

Magnetic integration based on high-frequency flux cancellation is a well-established technique for reducing the volume of multiple magnetic cores in multiphase voltage regulator applications for microprocessors [10]–[14]. Conventionally, integrated inductors are often fabricated in the form of coupled inductors [11]–[13], [15]–[17]. Due to the non-zero mutual inductances, the voltage and current of each constitutional inductor will interact with one another. Direct replacement of the two discrete inductors in the circuit shown in Fig. 2 with a coupled integrated inductor is not readily viable, because the resultant differential rectifier/inverter system will exhibit coupled system dynamics between i_{L1} and i_{L2}. Existing control of the rectifier will fail to work. New set of controllers which can decouple the interactions between i_{L1} and i_{L2} must be designed.

To simplify the controller design, an integrated inductor where its constitutional inductors are physically coupled on the same core but magnetically decoupled (without mutual coupling) is highly desirable. Existing works on developing decoupled magnetic integration have been reported for interleaved DC/DC converters based on high-frequency flux cancellation [14], [18]–[20]. The same concept has also been introduced in LCL filter design in inverter applications based on low-frequency flux cancellation, where the inductor currents are purely AC [21]. With these reported magnetic integration scheme, the core volume can be reduced by 14.4% for a single-phase inverter and 17.5% for a three-phase system.

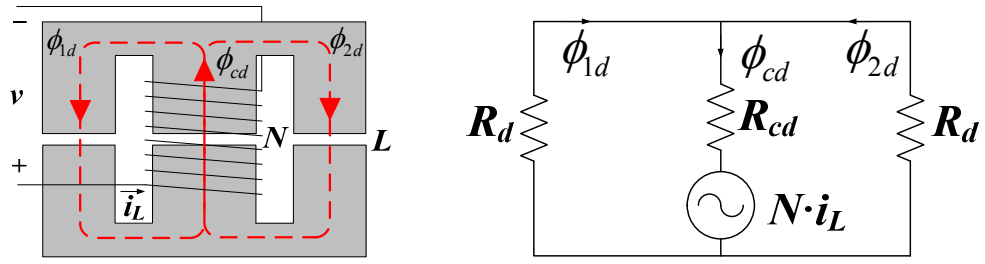
For Peer Review

In this paper, a new type of low-frequency integrated inductor without inductance coupling is proposed. The objective is to increase the power density of differential rectifiers/inverters by replacing their two bulky inductors with the proposed integrated inductor, while keeping the controller intact. This enables a plug-and-play installation of the proposed inductor to the original converter design with minimum system modifications. Different from existing low-frequency decoupled magnetic integration design, the proposed integrated inductor is applied in differential AC/DC or DC/AC conversion and has an AC plus DC current profile. The feasibilities for the magnetic integration under this scenario are firstly reported. Additionally, this paper provides an optimal design of the integrated inductor based on a complete set of dimensions of the magnetic core to achieve minimum core volume. Such a quantitative design method for low-frequency integrated magnetics has not been reported in prior arts. It will be demonstrated that, with proper optimization, a low-frequency integrated inductor can achieve more than 34.9% reduction in volume as compared to the discrete inductor. A thorough examination and comparison of the proposed integrated inductors are also carried out in this paper. This work is an extended version of [22].

II. Analysis of Conventional Discrete Inductor Design

One common structure for fabricating discrete inductors is the regular EE cores, where the windings are winded on the central leg (see Fig. 3(a)). Fig. 3(b) shows the equivalent magnetic circuit of the EE-core based inductor, where R_{cd} is the reluctance of the central leg (including the air gap), R_d is the reluctance of the two outer legs and yokes (including the air gaps), N is the turn's number of the winding, and ϕ_{1d}, ϕ_{2d}, and ϕ_{cd} are the magnetic fluxes in the outer legs and the central leg, respectively. The subscript d represents discrete inductor. Fig. 4 shows the full structure and dimensions of one pair of EE cores.

For Peer Review



(a) (b)

Fig. 3. (a) The structure of the discrete inductor and (b) its equivalent magnetic circuit.

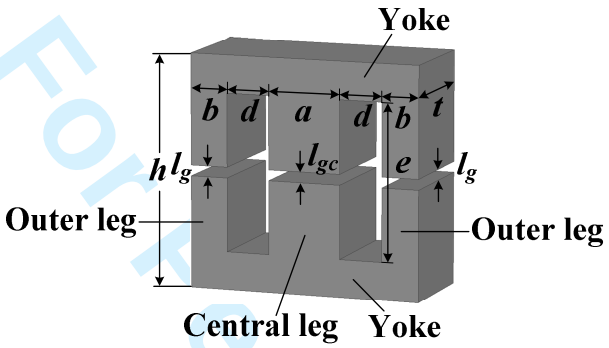


Fig. 4. The structure and dimensions of one pair of EE cores.

Based on Faraday's law (neglecting the winding resistances), one yields

$$v = N \cdot \frac{d\phi_{cd}}{dt}, \tag{1}$$

where v is the induced *emf* (which is equal to inductor's terminal voltage) that satisfies

$$v = L \cdot \frac{di_L}{dt}, \tag{2}$$

where L and i_L are respectively the inductance and current of the inductor. By combining (1) and (2), the flux in the central leg ϕ_{cd} can be expressed as

$$\phi_{cd} = \frac{Li_L}{N}. \tag{3}$$

Thus, the flux in the central leg is directly proportional to i_L.

The maximum flux ϕ_{cdm} and maximum flux density B_{cdm} in the central leg are thus

$$\phi_{cdm} = \frac{LI_{Lm}}{N}, \tag{4}$$

For Peer Review

$$B_{cdm} = \frac{\phi_{cdm}}{a_d t_d}, \tag{5}$$

where I_{Lm} is the peak current of i_{L1} and/or i_{L2}, and a_d and t_d are two dimensions of the core (see Fig. 4).

With reference to Fig. 3, the flux in the central leg ϕ_{cd} is split up into two identical parts in the two outer legs, so the maximum flux densities in the two outer legs B_{1dm} and B_{2dm} are

$$B_{1dm} = B_{2dm} = \frac{\phi_{cdm}}{2b_d t_d}. \tag{6}$$

In regular EE cores, the width of the central leg and that of the outer legs satisfy $a_d \approx 2b_d$. The maximum flux density in the central leg and that in the outer legs are thus identical. In practice, the maximum flux density in the core can be chosen at a value close to the saturation flux density B_{sat} of the core material, e.g. $B_{1dm} = B_{2dm} = B_{cdm} = 0.9B_{sat}$. For a given ϕ_{cdm} and B_{sat}, (5) and (6) specify the minimum dimensions of the core. Clearly, a larger inductor current I_{Lm} produces a higher ϕ_{cdm} which hence requires larger core dimensions and volume. Based on Fig. 4, the core volume (neglecting the volume of air gaps) of one pair of EE cores can be calculated as

$$V = [h \bullet (a + 2b + 2d) - 2ed]t, \tag{7}$$

and the overall core volume of the two identical discrete inductors V_d is

$$V_d = 2[h_d \bullet (a_d + 2b_d + 2d_d) - 2e_d d_d]t_d. \tag{8}$$

III. Proposed Low-Frequency Integrated Inductor Without Magnetic Coupling

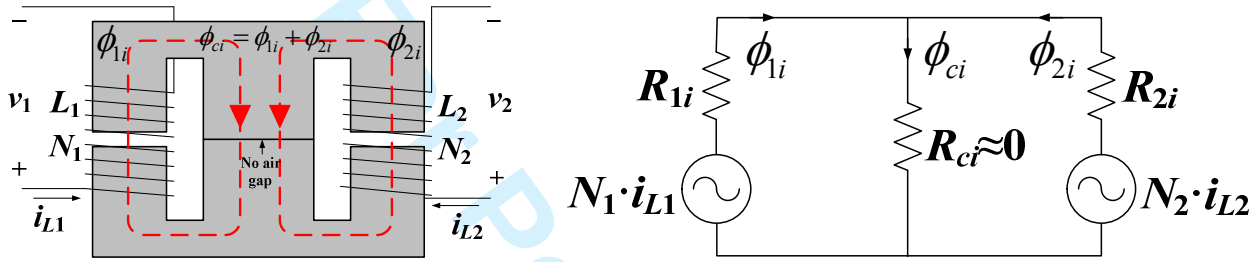
This section describes the proposed integrated inductor structure and its magnetic-decoupling principle. The feasibility of the core volume reduction through magnetic integration is also elaborated. The relationship between the mutual inductance and the core dimensions of the integrated inductor is also derived.

A. Criteria for Being a Magnetically Decoupled Integrated Inductor

The proposed integrated inductor structure and its equivalent magnetic circuit are illustrated in Fig. 5(a) and (b), respectively. L_1 and L_2 are the self-inductances of the two windings, N_1 and N_2 are their

For Peer Review

respective turn's numbers, R_{ci} is the reluctance of the central leg, R_{1i} and R_{2i} are the reluctances of the two outer legs and yokes (including the air gaps), and ϕ_{1i}, ϕ_{2i}, and ϕ_{ci} are the magnetic fluxes in the outer legs and the central leg, respectively. The subscript i represents the integrated inductor. As shown, the windings for L_1 and L_2 are wound on the outer legs sharing the same magnetic core. Without proper design, there could be strong magnetic coupling between them, leading to undesirable system operation. In order to design a magnetically decoupled integrated inductor, an analysis of the mutual inductance is needed.



(a) (b)

Fig. 5. (a) The structure and (b) the equivalent magnetic circuit of the integrated inductor.

Based on the coupled inductor model, the relationship of the voltages applied on the two windings and the inductor currents through them can be described as

$$\begin{cases} v_1 = L_1 \cdot \dfrac{di_{L1}}{dt} + M \cdot \dfrac{di_{L2}}{dt} \\ v_2 = M \cdot \dfrac{di_{L1}}{dt} + L_2 \cdot \dfrac{di_{L2}}{dt} \end{cases}, \tag{9}$$

where M is the mutual inductance, i_{L1} and i_{L2} are the currents through the two inductors, and v_1 and v_2 are the applied voltage across the two inductors, respectively, which can be expressed as,

$$\begin{cases} v_1 = N_1 \cdot \dfrac{d\phi_{1i}}{dt} \\ v_2 = N_2 \cdot \dfrac{d\phi_{2i}}{dt} \end{cases}. \tag{10}$$

On the other hand, according to the equivalent magnetic circuit shown in Fig. 5(b), one yields

$$\begin{cases} R_{1i} \cdot \phi_{1i} + R_{ci} \cdot (\phi_{1i} + \phi_{2i}) = N_1 \cdot i_{L1} \\ R_{2i} \cdot \phi_{2i} + R_{ci} \cdot (\phi_{1i} + \phi_{2i}) = N_2 \cdot i_{L2} \end{cases}. \tag{11}$$

For Peer Review

Solution of (9)–(11) gives the equation of the inductances of the integrated inductor as

$$\begin{cases} L_1 = \dfrac{N_1^2(R_{2i}+R_{ci})}{R_{1i}\cdot R_{ci}+R_{2i}\cdot R_{ci}+R_{1i}\cdot R_{2i}} \\ L_2 = \dfrac{N_2^2(R_{1i}+R_{ci})}{R_{1i}\cdot R_{ci}+R_{2i}\cdot R_{ci}+R_{1i}\cdot R_{2i}} \\ M = \dfrac{N_1\cdot N_2}{(R_{1i}+R_{2i})+(R_{1i}\cdot R_{2i})/R_{ci}} \end{cases}. \tag{12}$$

Equation (12) implies that $M = 0$ if $R_{ci} << R_{1i}R_{2i}$, which can be easily achieved by setting the length of the air gap in the central leg (l_{gc}) to zero while setting that for the outer legs to non-zero. As $M = 0$, the operation of the integrated inductor is electrically equivalent to that of two discrete and independent inductors.

Following a similar design procedure for the discrete inductor design, (12) can be used to estimate and design the magnetic core of the integrated inductor. To simplify the analysis, two assumptions are made:

(i) The permeability the core is sufficiently large, such that $R_{ci} \approx 0$;

(ii) The structure of the magnetic core is symmetrical, i.e.,

$$\begin{cases} N_1 = N_2 = N \\ R_{1i} = R_{2i} = R_i \\ L_1 = L_2 = L \end{cases}, \tag{13}$$

where

$$R_i = \frac{l_{gi}}{\mu_0 b_i t_i}. \tag{14}$$

Combining (12)–(14), L_1, L_2 and M are related to the core dimension following these relationships

$$\begin{cases} L_1 = L_2 = L = \dfrac{N^2\mu_0 b_i t_i}{l_{gi}} \\ M \approx 0 \end{cases}. \tag{15}$$

Therefore, the dimensions for the outer legs (e.g., t_i, b_i, and l_{gi}) can be determined given the inductance of L_1 and L_2.

For Peer Review

B. Feasibility of Core Volume Reduction by Shrinking the Central Leg

Since $M = 0$, the fluxes of the two outer legs can be calculated as

$$\phi_{1i} = \frac{Li_{L1}}{N}, \tag{16}$$

$$\phi_{2i} = \frac{Li_{L2}}{N}. \tag{17}$$

Therefore, ϕ_{ci} which is the sum of ϕ_{1i} and ϕ_{2i} is

$$\phi_{ci} = \phi_{1i} + \phi_{2i} = \frac{L(i_{L1} + i_{L2})}{N} = \frac{Li_o}{N}. \tag{18}$$

It should be noted that, unlike the fluxes in the discrete inductors as derived in (4) which are proportional to i_{L1} and i_{L2}, the flux in the central leg of the integrated inductor is proportional to i_o which is purely DC (with small switching frequency ripple) provided that active power-decoupling control is employed. In other words, the large AC components in ϕ_{1i} and ϕ_{2i} in the outer legs are canceled in the central leg, and ϕ_{ci} is almost DC with a much smaller amplitude than that of the outer legs. Intuitively, the cross-sectional area in the central leg can be shrunk dramatically before the core gets saturated. The volume of the integrated inductor can hence be reduced.

C. Exact Examination of the Coupling Coefficient

In practice, R_{ci} always exhibits a finite value which might become quite significant for an integrated inductor as the width of the central leg is shrunk. The assumptions made in Section III-A (i.e., $R_{ci} << R_{1i}R_{2i}$) might be violated and the coupling between L_1 and L_2 can be substantial. Therefore, a careful examination of the coupling effect with respect to the width of the center leg is also needed.

The coupling coefficient k of an integrated inductor is defined as

$$k = M / \sqrt{L_1 L_2} = M / L. \tag{19}$$

Therefore, according to (12) and (13), k can be expressed as

$$k = M / L = \frac{R_{ci}}{R_i + R_{ci}}, \tag{20}$$

For Peer Review

where R_i and R_{ci} now incorporates the reluctances of both the magnetic core and the air gaps. The effective magnetic path is chosen as the central path of the magnetic core. According to Fig. 5, we have

$$R_{ci} = \frac{e_i + (h_i - e_i)/2}{\mu a_i t_i} = \frac{h_i + e_i}{2\mu a_i t_i}, \tag{21}$$

$$\begin{aligned} R_i &= \frac{l_{gi}}{\mu_0 b_i t_i} + \frac{e_i + (h_i - e_i)/2 - l_{gi}}{\mu b_i t_i} + \frac{d_i + a_i/2 + b_i/2}{\mu t_i (h_i - e_i)/2} \times 2 \\ &= \frac{l_{gi}\mu(h_i - e_i) + [(h_i + e_i)/2 - l_{gi}]\mu_0(h_i - e_i) + 2\mu_0 b_i(2d_i + a_i + b_i)}{\mu_0 \mu b_i t_i (h_i - e_i)}, \end{aligned} \tag{22}$$

where μ is the permeability of the magnetic core.

Substitution of (21) and (22) into (23) leads to

$$k = \frac{R_{ci}}{R_i + R_{ci}} = \frac{1}{1 + \frac{R_i}{R_{ci}}} = \frac{1}{1 + \frac{2a_i\{l_{gi}\mu(h_i - e_i) + [(h_i + e_i)/2 - l_{gi}]\mu_0(h_i - e_i) + 2\mu_0 b_i(2d_i + a_i + b_i)\}}{\mu_0 b_i (h_i^2 - e_i^2)}}. \tag{23}$$

According to (23), the relationship of the coupling coefficient k and the width of central leg a_i is plotted in Fig. 6. Here, TDK N87 ferrite [23] is chosen as the magnetic core (where μ=1700μ_0). The total height of the core h_i and the height of the window e_i are set equal to that of the discrete inductors (i.e., h_i=h_d, and e_i=e_d), for which a TDK E70 core (see Table I [23]) is selected.

In Fig. 6(a), the total widths of the core (i.e., a_i+2b_i+2d_i) and that of the outer legs b_i are set equal to those of a TDK E70 core, respectively; while in Fig. 6(b), the ratio of a_i/b_i and the width of the window d_i are set as a_i/b_i=I_{om}/I_{Lm} and d_i=d_d. Based on Fig. 6(a) and (b), we can make the following observations:

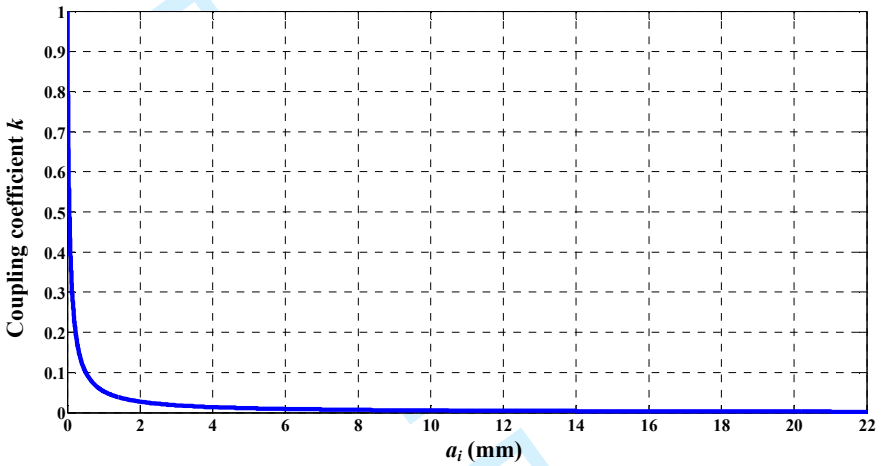
(i) In both cases, the coupling coefficient k is increasing monotonically with the decrease of a_i.

(ii) In the first case, when the total width and the outer legs of the core is fixed, k is a strong function of a_i. In particular, when a_i varies from zero to a substantially large value (e.g. 22 mm), k varies from 1 (fully coupled) to almost zero (fully decoupled).

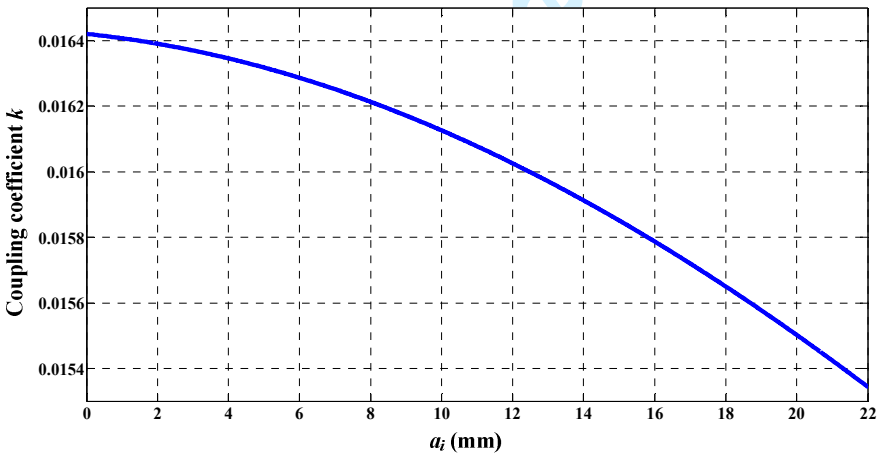
For Peer Review

(iii) In the second case when the ratio of a_i/b_i and the width of the window d_i are fixed, k is almost invariant against the change of a_i. Moreover, k is sufficiently small (≈0.016) and can be regarded as quasi-fully decoupled.

Equation (23) and Fig. 6 are useful for determining the minimum a_i given the maximum coupling requirement and the core-volume-optimization method, as will be discussed in Section IV. For instance, if a_i is the only optimizing variable in the core design and if the maximum coupling coefficient is 0.1, then based on (23) and Fig. 6(a), the minimum a_i can be determined as 0.5 mm.



(a)



(b)

Fig. 6. The relationship of coupling coefficient and the width of central leg a_i when (a) $h_i=h_d$, $e_i=e_d$, $b_i=b_d$ and $a_i+2b_i+2d_i = a_d+2b_d+2d_d$, (b) $h_i=h_d$, $e_i=e_d$, $a_i/b_i=I_{om}/I_{Lm}$ and $d_i=d_d$.

IV. Volume Optimization for the Integrated Inductor

In Section III, the feasibility of volume reduction for the proposed integrated inductor by shrinking the center leg has been demonstrated. In this section, two volume optimization methods are carried out and compared in terms of achieving maximum core volume reduction.

A. Volume Optimization by Shrinking the Central Leg

In this part, a volume optimization study based on shrinking only the central leg of the integrated inductor is conducted. According to (15)–(17), the maximum fluxes ϕ_{1im} and ϕ_{2im}, and the associated maximum flux densities B_{1im} and B_{2im} in the two outer legs are

$$\phi_{1im} = \phi_{2im} = \frac{LI_{Lm}}{N} = N \bullet I_{Lm} \bullet \frac{\mu_0 b_i t_i}{l_{gi}}, \tag{24}$$

$$B_{1im} = B_{2im} = \frac{\phi_{1im}}{b_i t_i} = N \bullet I_{Lm} \bullet \frac{\mu_0}{l_{gi}}. \tag{25}$$

In addition, according to (15) and (18), the maximum flux ϕ_{cim} and maximum flux density B_{cim} in the central leg are

$$\phi_{cim} = \frac{LI_{om}}{N} = N \bullet I_{om} \bullet \frac{\mu_0 b_i t_i}{l_{gi}}, \tag{26}$$

$$B_{cim} = \frac{\phi_{cim}}{a_i t_i} = N \bullet I_{om} \bullet \frac{\mu_0}{l_{gi}} \bullet \frac{b_i}{a_i}, \tag{27}$$

where I_{om} is the maximum value of the output current i_o.

To maximally shrink the central leg, the maximum flux density in the outer legs and the central leg should be kept the same and close to the saturation flux density of the core material, e.g., $B_{1im} = B_{2im} = B_{cim} = 0.9B_{sat}$.

Therefore, the combination of (25) and (27) yields

$$\frac{a_i}{b_i} = \frac{I_{om}}{I_{Lm}}. \tag{28}$$

For Peer Review

Equation (28) shows that if I_{om}<<I_{Lm}, then the width of the central leg a_i can be reduced greatly and will be much smaller than the width of the outer legs b_i.

Assume that the inductance L and the winding turn's number N are kept the same for both the discrete inductors and the integrated inductor in this work. Based on (4) and (24), one yields

$$\phi_{cdm} = \phi_{1im}. \tag{29}$$

As mentioned above, $B_{1dm} = B_{2dm} = B_{cdm} = B_{1im} = B_{2im} = 0.9B_{sat}$. Equalizing (6) and (25) leads to

$$b_i t_i = 2b_d t_d, \tag{30}$$

which indicates that the cross-sectional area of the two outer legs in the integrated inductor should be doubled of that of the discrete ones. For ease of construction, here we choose b_i=b_d, t_i=2t_d. The height and total length of the discrete inductors and the integrated inductor are kept the same, i.e., e_i=e_d, h_i=h_d, a_i+2b_i+2d_i=a_d+2b_d+2d_d. Therefore, after a one-dimensional optimization of the central leg, the integrated inductor core volume is

$$V_i = [h_i \bullet (a_i + 2b_i + 2d_i) - 2e_i d_i] \bullet t_i = [h_d \bullet (a_d + 2b_d + 2d_d) - 2e_d \bullet \frac{a_d + 2b_d - \frac{I_{om}}{I_{Lm}} \bullet b_d}{2}] \bullet 2t_d. \tag{31}$$

B. Volume Optimization by Considering All the Core Dimensions

To achieve maximum core volume reduction, a method of volume optimization process which takes into consideration all the dimensions of the magnetic core is carried out in this section.

The maximum flux density in the two yokes is

$$B_{yim} = \frac{\phi_{1im}}{\frac{h_i - e_i}{2} \bullet t_i}. \tag{32}$$

For minimum core volume design, the maximum flux density in all the parts of the integrated inductor core should be kept the same and close to the saturation flux density, e.g., $B_{1im} = B_{2im} = B_{yim} = B_{cim} = 0.9B_{sat}$.

By equalizing (25) and (32), one obtains

For Peer Review

$$b_i = \frac{h_i - e_i}{2}. \tag{33}$$

To ensure enough winding area of the integrated inductor, the window area of the integrated inductor should be the same as that of the discrete inductors, i.e.,

$$d_i e_i = d_d e_d . \tag{34}$$

Substitution of the dimension relationships in (28), (30), (33), and (34) into (7) yields the expression of the integrated inductor core volume as

$$V_i = [h_i \bullet (a_i + 2b_i + 2d_i) - 2e_i d_i] \bullet t_i = 2b_d t_d [2(1 + \frac{2I_{Lm}}{I_{om}})a_i + \frac{4d_d e_d}{e_i} + (\frac{I_{om}}{I_{Lm}} + 2)e_i], \tag{35}$$

which reveals that the volume V_i is reduced to a function involving only two dimensional variables a_i and e_i for a full-dimensional optimzation of the proposed integrated inductor.

C. Case Study

In this paper, a pair of E70 cores from TDK Company is used to fabricate the discrete inductors. The dimensions of one pair of E70 cores are shown in Table I.

TABLE I. THE DIMENSIONS OF A PAIR OF E70 CORES

Symbol	Value (mm)
a_d	22
b_d	11.25
d_d	13
e_d	43.8
h_d	66.4
t_d	32

Then, the overall core volume of the two identical discrete inductors V_d=226713.6 mm^3.

From Fig. 2(b), one can obtain that I_{om}/I_{Lm}=0.302. Therefore, with reference to Table I, after volume optimization by only shrinking the central leg, the core volume of the integrated inductor is 174574.1 mm^3, which achieves 23.0% core volume reduction as compared to the two discrete inductors.

For volume optimization by considering all the dimensions, and by substituting the dimensions of Table I into (35), the volume of the integrated inductor is

For Peer Review

$$V_i = 10976.42a_i + \frac{1639872}{e_i} + 1657.44e_i \text{ mm}^3, \tag{36}$$

which has a minimum value when

$$\frac{1639872}{e_i} = 1657.44e_i \Rightarrow e_i = 31.5 \text{ mm}, \tag{37}$$

and

$$V_i = 10976.42a_i + 104268.8 \text{ mm}^3. \tag{38}$$

When a_i approaches zero, $V_{i_theoretical_min}$=104268.8 mm^3. The maximum reduction of the magnetic core volume is therefore

$$\Delta V\%_{max} = \frac{V_d - V_{i_theoretical_min}}{V_d} \times 100\% = 54.0\%. \tag{39}$$

Fig. 7 shows the calculated core volume of the integrated inductor versus a_i and e_i, which is consistent with the anlaysis above.

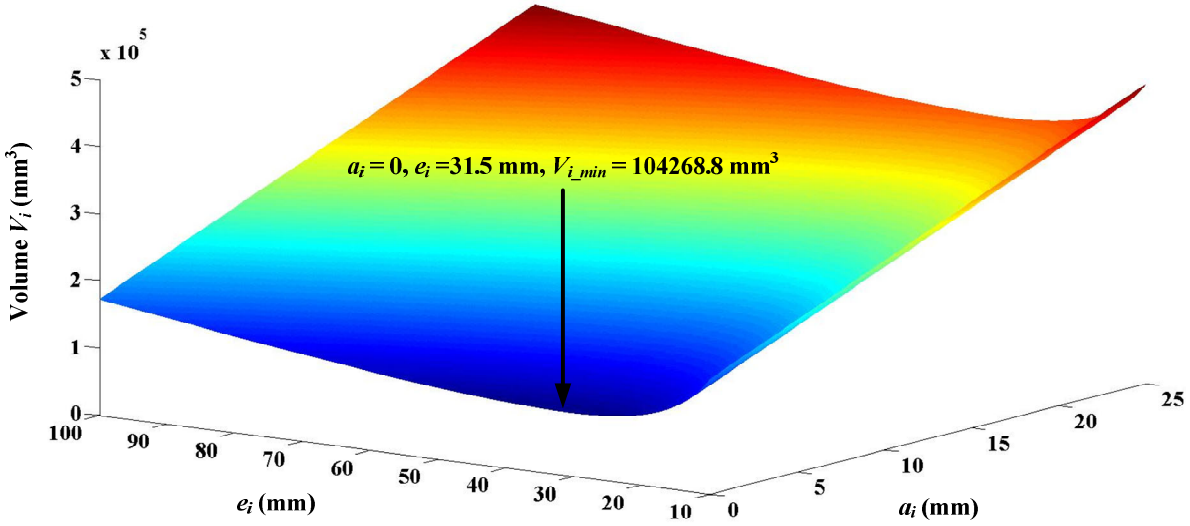


Fig. 7. The relationship of the integrated inductor core volume and the dimensions a_i and e_i.

For a practical design, a_i cannot approach zero as assumed in (39). Not only will the mechanical stability of the core be weakened, the coupling between L_1 and L_2 will also be increased which is undesirable for system operation. Additionally, for ease of construction, the optimal e_i in (37) is not used here, and a proof-of-concept prototype with b_i and e_i being the same as that of the discrete

inductors is selected for the volume optimization. In particular, $a_i=b_i*I_{om}/I_{Lm}$=3.4 mm, $e_i = e_d$ = 43.8 mm (closed to the optimal e_i in (37)), $t_i=2t_d$=64 mm, $d_i=d_d$=13 mm, and $h_i=h_d$=13 mm, which leads to V_i=147671.0 mm^3. The volume reduction of the magnetic core based on this suboptimal integrated inductor design is

$$\Delta V\%_{max} = \frac{V_d - V_i}{V_d} \times 100\% = 34.9\%. \quad (40)$$

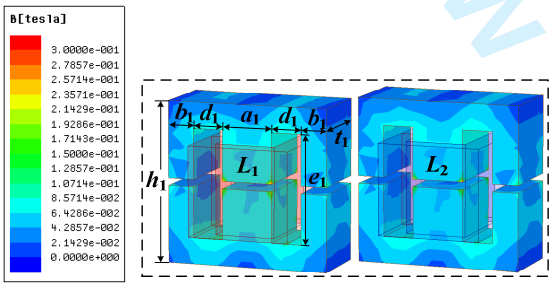
Compared with the results of that with the one-dimensional design method, a much smaller core volume is achieved with the full-dimensional optimization method.

V. Simulation Verification of The Size Reduction

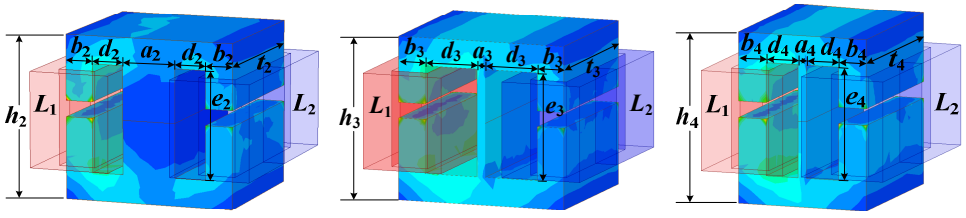
The Finite Element Analysis software Maxwell is used to simulate the flux density distribution of the magnetic cores. Inductor specifications for both the discrete inductors and the proposed integrated inductors are given in Table II. In particular, the inductors are driven by two current sources identical to i_{L1_avg} and i_{L2_avg} (i.e., averaged i_{L1} and i_{L2} over one switching period), as shown in Fig. 2(b), without considering the switching-frequency current ripples.

TABLE II. SPECIFICATIONS FOR BOTH DISCRETE INDUCTORS AND INTEGRATED INDUCTOR

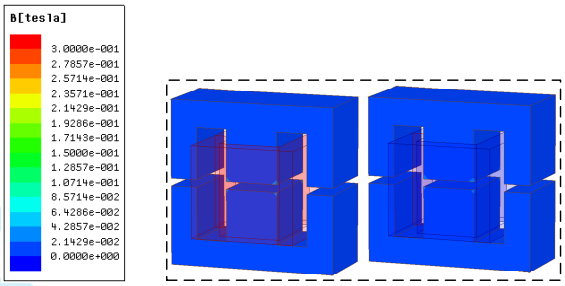
Core material	TDK N87 ferrite cores
Inductance L_1, L_2 (mH)	3.5
Winding turn's number N	117
Fundamental frequency of i_{L1} and i_{L2} (Hz)	50
Maximum flux density of the core B_m (T)	0.3



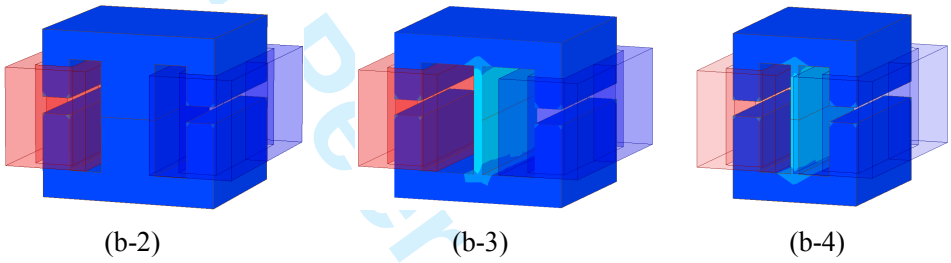
(a-1)



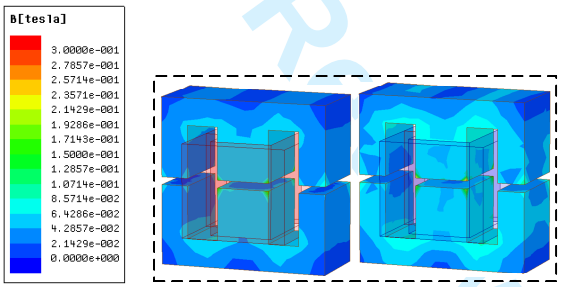
(a-2) (a-3) (a-4)



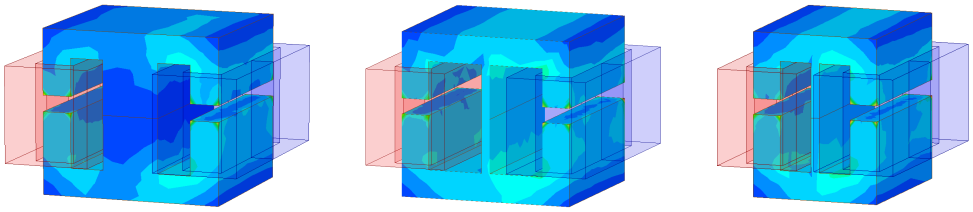
(b-1)



(b-2) (b-3) (b-4)



(c-1)



(c-2) (c-3) (c-4)

For Peer Review

Fig. 8. Flux density distributions of identical discrete inductors #1((a-1), (b-1), (c-1)), integrated inductor #2((a-2), (b-2), (c-2)), integrated inductor with shrunk leg #3((a-3), (b-3), (c-3)), and optimized integrated inductor #4((a-4), (b-4), (c-4)) at time instance of (a) T_1, (b) T_2, and (c) T_3 of Fig. 2(b).

Four types of inductors are modeled and compared in the simulation, where #1 are two identical discrete inductors, #2 is an integrated inductor without core volume reduction, #3 is an integrated inductor by only shrinking the central leg, and #4 is an optimized integrated inductor. The detailed dimensions of the four models are tabulated in Table III and shown in Fig. 8, where the red winding represents L_1 and the blue winding represents L_2.

TABLE III. THE DIMENSIONS OF #1–#4 IN MAXWELL SIMULATIONS

#1		#2		#3		#4	
Symbol	Value (mm)	Symbol	Value (mm)	Symbol	Value (mm)	Symbol	Value (mm)
a_1	22	a_2	22	a_3	3.4	a_4	3.4
b_1	11.25	b_2	11.25	b_3	11.25	b_4	11.25
d_1	13	d_2	13	d_3	22.3	d_4	13
e_1	43.8	e_2	43.8	e_3	43.8	e_4	43.8
h_1	66.4	h_2	66.4	h_3	66.4	h_4	66.4
t_1	32	t_2	64	t_3	64	t_4	64

In Fig. 8, the flux density of the four types of cores are captured at three instances of Fig. 2(b), i.e., at T_1 when i_{L1_avg} is at its maximum, at T_2 when i_{L1_avg} and i_{L2_avg} intersect with each other, and at T_3 when i_{L2_avg} is maximum.

By comparing the simulated results of #1 and #2 in Fig. 8(a) and Fig. 8(b), it can be seen that the #1 inductors exhibit a high flux density that is distributed among the cores at T_1 and T_2. In contrast, after initial magnetic integration in #2, it can be seen that the flux density in the central leg is always kept at a low level, even though that of the outer legs are significantly larger.

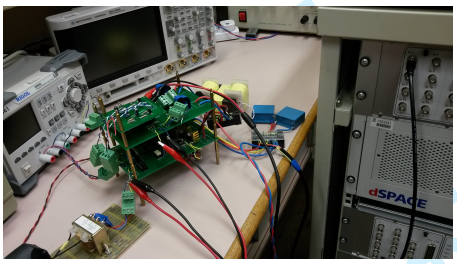
In #3, the center leg is further shrunk and the total width of the core is not changed. According to the analysis in Section IV, a decrease of a_i will cause the flux density in the center leg to increase. Fig. 8(c) shows that, however, the flux density in the central leg is still kept below B_m 0.3 T throughout the whole operating period. In this design example, a core volume reduction of 23.0% as compared to that of #1 has been achieved.

Finally, the core of #3 is further optimized as #4, which has the same window area as #1 but a smaller total width as compared to #1–#3. Fig. 8(d) confirms that the flux density in all parts of the core is lower than B_m. Therefore, #4 core can still operate properly without magnetic saturation.

For Peer Review

VI. Experimental Verifications

A differential buck rectifier circuit as shown in Fig. 9(a) is constructed to examine the performance of the proposed low-frequency integrated inductors. The system is operated with v_{ac} =110 Vrms/50 Hz and V_o = 43.6 V. Two bang-bang controllers are designed and employed to control the inductor currents such that the switching frequency is around 20 kHz [2]. In addition, the inductor waveform control [2] is implemented to achieve active power decoupling function. The four inductor prototypes corresponding to the simulation models are shown in Fig. 9(b), where TDK N87 ferrite cores [23] are used as they have low core losses at high switching frequencies. In particular, for mechanical stability and easy production, the width of the central leg for #3 core is designed as a_3=5.5 mm, which is 2.1 mm wider than that in the simulation. This leads to a slightly lesser volume reduction (i.e., 20.4%) as compared to that achieved in the simulations. For the same reason, the width of the central leg for #4 core is chosen as a_4=a_3=5.5 mm. The total core volume of #4 is reduced by 30.9% as compared to the total volume of the two discrete inductors.



(a)



(b)

Fig. 9. (a) Experiment setup of the differential buck rectifier and (b) the inductor prototypes (from left to right: the two discrete inductors #1, the integrated inductors #2, the integrated inductors with shrunk leg #3 and the optimized integrated inductor #4).

The steady-state operating waveforms of the inductor currents (i_{L1} and i_{L2}) and the output voltage (V_o) of the buck rectifier with each of the four types of inductors are shown in Fig. 10 (a)–(d). It can be seen that the inductor currents and the output voltage waveforms are almost identical in all the scenarios with the same controllers, and the integrated inductors are operating just like two discrete inductors. These results indicate that the operation of the differential buck rectifier is not altered by the use of the proposed integrated inductors.

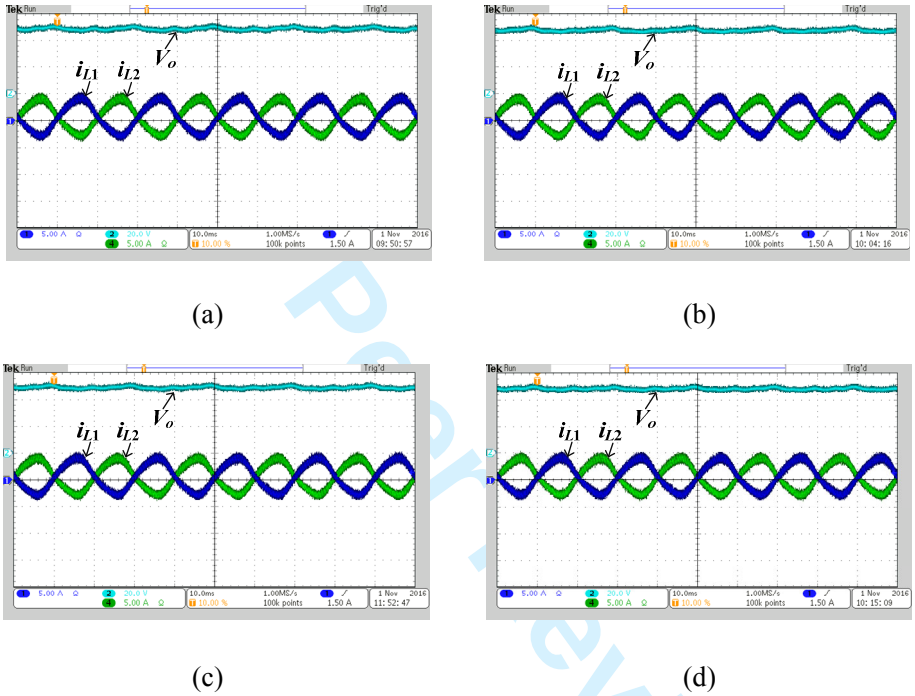


Fig. 10. Experimental waveforms with (a) discrete inductors, (b) integrated inductor, (c) integrated inductor with shrunk leg and (d) optimized integrated inductor.

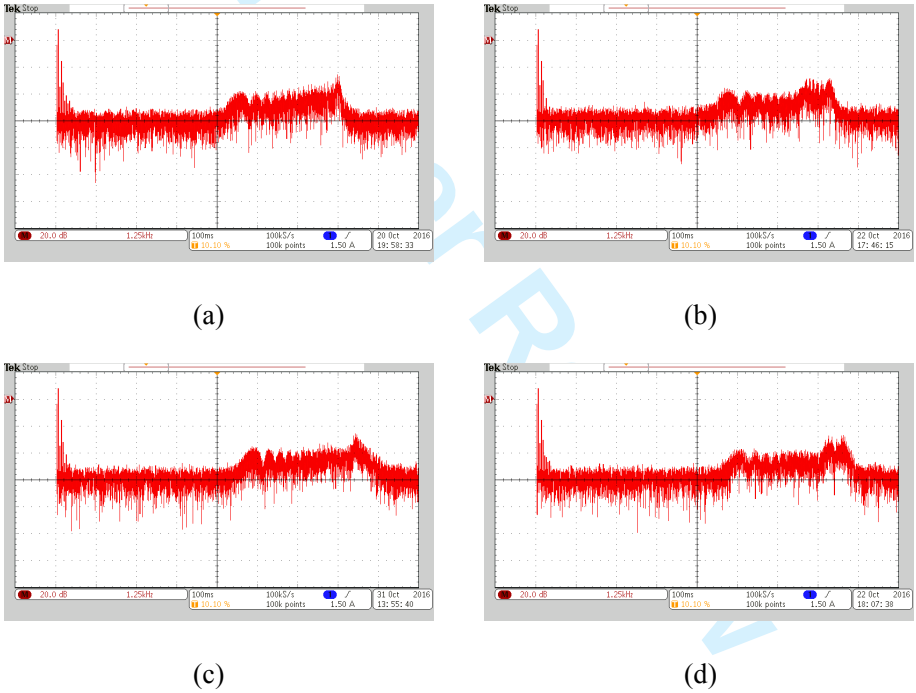
The measured coupling coefficient k of the four types of inductors is shown in Table III, where it is evident that the reduction of the width of the center leg increases k. Nonetheless, k is kept less than 0.1, which is an expected result and which will not affect the normal operation of the system.

The power efficiency performances of the differential buck rectifier with the four types of inductors are also recorded in Table IV. A slight drop of power efficiency is observed by comparing the integrated inductors (#2–#4) to #1. Although the integrated inductors are expected to have reduced core losses due to the reduced core volume, the length of the windings increases (i.e., $t_2 = t_3 = t_4 = 2t_1$) as

compared to that in #1, and hence more copper losses. Fortunately, the power efficiency of the whole system with the proposed integrated inductors is comparable to that with the discrete inductors. An additional observation is that the energy efficiencies with the three integrated inductors are almost identical.

TABLE IV. SOME CHARACTERISTICS OF THE FOUR TYPES OF INDUCTORS

Inductor type	Coupling coefficient	Circuit efficiency	Maximum switching frequency (kHz)	Steady-state temperature (°C)
Discrete inductors #1	0	87.15%	9.107	29.3
Integrated inductor #2	0.023	86.07%	9.294	31.3
Integrated inductor with shrunk leg #3	0.082	86.02%	10.012	29.8
Optimized integrated inductor #4	0.087	85.97%	10.288	34.4



(a) (b) (c) (d)

Fig. 11. FFT analysis of inductor current i_{L1} of (a) discrete inductors, (b) integrated inductor, (c) integrated inductor with shrunk central leg and (d) optimized integrated inductor.

The maximum switching frequency of the circuit with the four types of inductors are also measured and shown in Table III. It can be seen that the maximum switching frequency increases slightly as the coupling effect α increases. The reason is that the mutual inductance reduces the effective inductance of L_1 and L_2. According to $Ldi/dt=V$, a smaller inductance will lead to a sharper rising/falling slope and

hence a faster switching frequency given a fixed ripple band. Fig. 11 shows the FFT measurements of the inductor current i_{L1} of the four types of inductors. It can be seen that the fundamental frequency of i_{L1} is 50 Hz and that there are also substantial high-order harmonics due to the operation of active power decoupling function. The increase of the switching frequency after magnetic integration can also be observed at the high-frequency range of the FFT results given in Fig. 11.

Finally, the thermal performance of the proposed integrated inductors are examined. A data logger probing at six different test points (see Fig. 12) is used. In particular, the measurements are taken after three hours of operation at 22 °C ambient temperature with free convection. The average temperatures of the six test points for the four types of inductors are recorded in Table IV. The results show that after magnetic integration, the core temperature rises as compared to the discrete inductors. The rise of the core temperature is generally due to (i) the reduced surface area for heat dissipation which increases the thermal resistance of the inductor, and (ii) the increased power losses in the windings as the windings of the integrated inductor are longer than the windings of the discrete inductors. A further examination of the measurement results shows that #3 has the lowest core temperature among the integrated inductors and is comparable to that of #1, while the core temperature for #4 is the highest. The reason is that #3 has the largest surface area for heat dissipation due to a larger window size, while #4 has the minimum surface area.

Fig. 13 shows the captured the steady-state thermal images of the four types of inductors. The images are in conformity to the steady-state temperature shown in Table IV.

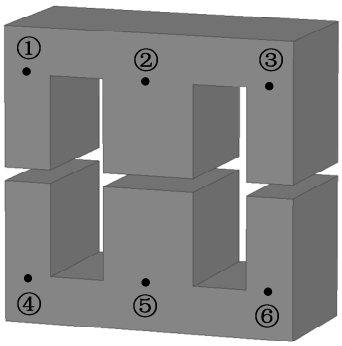
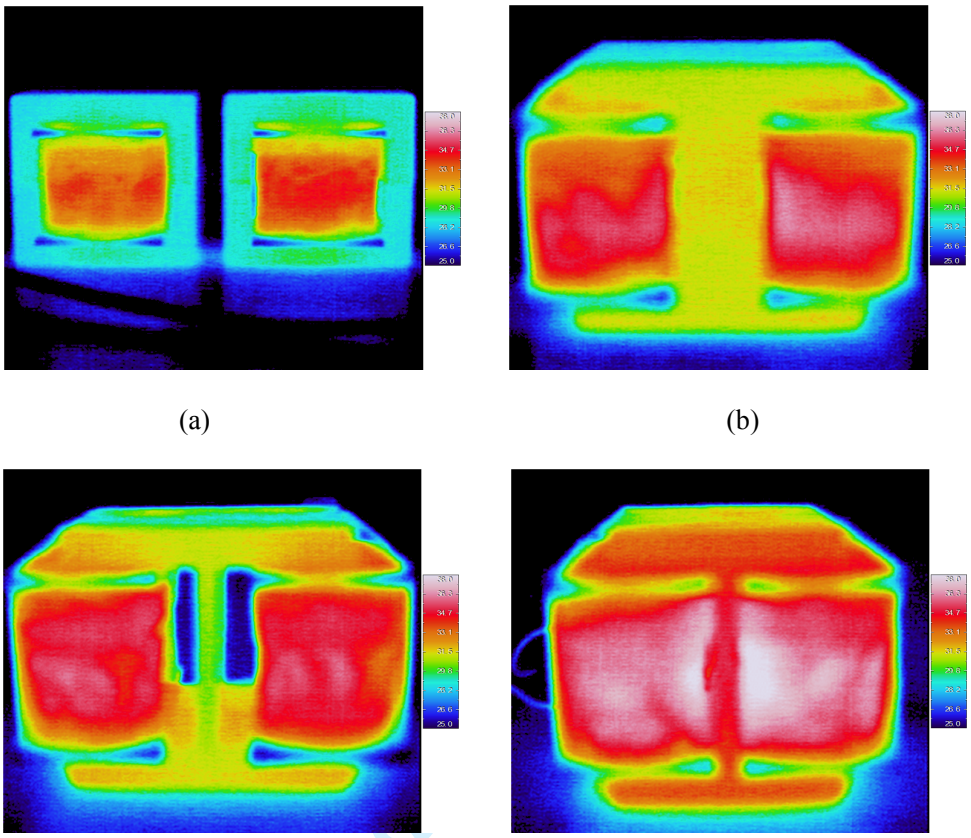


Fig. 12. The temperature test points of the inductor core.

For Peer Review



(a) (b)

(c) (d)

Fig. 13. Thermal images of (a) discrete inductors, (b) integrated inductor, (c) integrated inductor with shrunk central leg and (d) optimized integrated inductor.

VII. Conclusions

A type of low-frequency integrated inductor based on common EE core, without magnetic coupling, for improving the power density of differential rectifiers/inverters, is proposed in this paper. The principles of the proposed low-frequency magnetic integration and major design considerations are provided. Theoretical analysis shows that up to 54.0% of core volume reduction might be achieved with the proposed integrated inductor with the same turn's number of the windings as compared to that with using two discrete inductors. An integrated inductor with 34.9% reduction in volume is designed and verified in Maxwell. The performance of several integrated inductors with up to 30.9% reduction in volume are also constructed and examined experimentally. The proposed magnetic integration design method can be extended to other converter designs that involve two or more low frequency AC and/or AC+DC inductors.

REFERENCES

[1] R. O. Caceres and I. Barbi, "A boost DC-AC converter: analysis, design, and experimentation," *IEEE Transactions on Power Electronics*, vol. 14, no. 1, pp. 134-141, Jan 1999.

[2] S. Li, G. R. Zhu, S. C. Tan, and S. Y. Hui, "Direct AC/DC rectifier with mitigated low-frequency ripple through inductor-current waveform control," *IEEE Transactions on Power Electronics*, vol. 30, no. 8, pp. 4336-4348, Aug. 2015.

[3] W. Yao, X. Wang, P. Loh, X. Zhang, and F. Blaabjerg, "Improved power decoupling scheme for single-phase grid-connected differential inverter with realistic mismatch in storage capacitances," *IEEE Transactions on Power Electronics*, no.99, pp.1-1.

[4] G. R. Zhu, S. C. Tan, Y. Chen, and C. K. Tse, "Mitigation of low-frequency current ripple in fuel-cell inverter systems through waveform control," *IEEE Transactions on Power Electronics*, vol. 28, no. 2, pp. 779-792, Feb. 2013.

[5] M. Tampubolon, I. Purnama, P. C. Chi, J. Y. Lin, Y. C. Hsieh, and H. J. Chiu, "A DSP-based differential boost inverter with maximum power point tracking," in *IEEE ECCE Asia*, 2015, pp. 309-314.

[6] W. Yao, X. Wang, X. Zhang, Y. Tang, P. C. Loh, and F. Blaabjerg, "A unified active damping control for single-phase differential mode buck inverter with LCL-filter," in *IEEE 6th International Symposium on PEDG*, 2015, pp. 1-8.

[7] K. Jha, S. Mishra, and A. Joshi, "High-quality sine wave generation using a differential boost inverter at higher operating frequency," *IEEE Transactions on Industry Applications*, vol. 51, no. 1, pp. 373-384, Jan.-Feb. 2015.

[8] I. E. Colling and I. Barbi, "Reversible unity power factor step-up/step-down AC-DC converter controlled by sliding mode," *IEEE Transactions on Power Electronics*, vol. 16, no. 2, pp. 223-230, Mar. 2001.

[9] W. Yao, X. Zhang, X. Wang, Y. Tang, P. C. Loh, and F. Blaabjerg, "Power decoupling with autonomous reference generation for single-phase differential inverters," in *EPE'15 ECCE-Europe*, 2015, pp. 1-10.

[10] P. Zumel, O. Garcia, J. A. Cobos, and J. Uceda, "Magnetic integration for interleaved converters," in *Proc. IEEE Appl. Power Electron. Conf. Expo*., 2003, pp. 1143–1149.

[11] P. L. Wong, P. Xu, B. Yang, and F. C. Lee, "Performance improvements of interleaving VRMs with coupling inductors," *IEEE Transactions on Power Electronics*, vol. 16, no. 4, pp. 499-507, Jul. 2001.

[12] Y. Yang, Y. Dong and F. C. Lee, "A new coupled inductors design in 2-phase interleaving VRM," *2009 IEEE 6th International Power Electronics and Motion Control Conference*, 2009, pp. 344-350.

[13] H. Li, Z. Chen and Y. Yang, "Application study of multi-phase coupled array integrated magnetic in VRM," *The 2nd International Symposium on Power Electronics for Distributed Generation Systems*, 2010, pp. 214-219.

[14] W. Chen, F. C. Lee, X. Zhou, and P. Xu, "Integrated planar inductor scheme for multi-module interleaved quasi-square-wave (QSW) DC/DC converter," in *IEEE PESC*, 1999, pp. 759-762.

[15] P. W. Lee, Y. S. Lee, D. K. W. Cheng, and X. C. Liu, "Steady-state analysis of an interleaved boost converter with coupled inductors," *IEEE Transactions on Industrial Electronics*, vol. 47, no. 4, pp. 787-795, Aug. 2000.

[16] M. Mu, F. C. Lee, Y. Jiao, and S. Lu, "Analysis and design of coupled inductor for interleaved multiphase three-level DC-DC converters," in *Proc. IEEE Appl. Power Electron. Conf. Expo*., 2015, pp. 2999-3006.

[17] J. Li, C. R. Sullivan, and A. Schultz, "Coupled inductor design optimization for fast-response low-voltage DC–DC converters," in *Proc. IEEE Appl. Power Electron. Conf. Expo*., 2002, pp. 817–823.

[18] C. C. Huang, Y. C. Liu, T. F. Pan, P. J. Tseng, C. H. Chang, Y. K. Lo, and H. J. Chiu, "Study on an interleaved buck power factor corrector with GaNFET and integrated inductor," in *IFEEC*, 2013, pp. 30-35.

[19] S. Y. Lee, A. G. Pfaelzer, and J. D. van Wyk, "Comparison of different designs of a 42-V/14-V DC/DC converter regarding losses and thermal aspects," *IEEE Transactions on Industry Applications*, vol. 43, no. 2, pp. 520-530, Mar.-Apr. 2007.

[20] K. Yao, M. Ye, M. Xu, and F. C. Lee, "Tapped-inductor buck converter for high-step-down DC-DC conversion," *IEEE Transactions on Power Electronics*, vol. 20, no. 4, pp. 775-780, Jul. 2005.

For Peer Review

[21] D. Pan, X. Ruan, C. Bao, W. Li and X. Wang, "Magnetic integration of the LCL filter in grid-connected inverters," *IEEE Transactions on Power Electronics*, vol. 29, no. 4, pp. 1573-1578, Apr. 2014.

[22] M. Wu, S. Li, S. C. Tan, and S. Y. Hui, "Integrated magnetics for power density improvement of differential rectifiers and inverters," in *IEEE SPEC*, 2016, pp. 1-6.

[23] *Ferrites and accessories, E70/33/32 Core and accessories*, TDK Company, 2013.

For Peer Review